On the effect of water-induced degradation of thin-film piezoelectric microelectromechanical systems

Runar Plünnecke Dahl-Hansen, *Member IEEE,* Frode Tyholdt, Jo Gjessing, Andreas Vogl, Paul Wittendorp, Jon Vedum, *Member IEEE*, and Thomas Tybell

Abstract - **Lifetime and reliability in realistic operating conditions are important parameters for the application of thin-film piezoelectric microelectromechanical systems (piezoMEMS) based on lead zirconate titanate (PZT). Humidity can induce time-dependent dielectric breakdown at a higher rate compared to dry conditions, and significantly alter the dynamic behavior of piezoMEMS-devices. Here we assess the lifetime and reliability of PZT-based micromirrors with and without humidity barriers operated at 23 ºC in an ambient of 0 and 95 % relative humidity. The correlation of the dynamic response, as well as the ferroelectric, dielectric, and leakage properties, with degradation time was investigated. In humid conditions, the median time-to-failure was increased from $2.7x10^4$ $[1.9x10^4 - 4.0x10^4]$ s to $1.1x10^6$ $[0.9x10^6 - 1.5x10^6]$ s at 20 V_{AC} continuous unipolar actuation, by using a 40 nm thick Al_2O_3 humidity barrier. However, the initial maximum angular deflection, polarization, and dielectric permittivity decreased by about 6, 11, and 12 %, respectively, for Al_2O_3 capped devices. For both bare and encapsulated devices, the onset of electrothermal breakdown-events was the dominant cause of degradation. Severe distortions in the device's dynamic behavior, together with failure from loss of angular deflection, preceded time-dependent dielectric breakdown in 95 % relative humidity. Moreover, due to the film-substrate stress transfer sensitivity of thin-film devices, water-induced degradation affects the reliability of thin-film piezoMEMS differently than bulk piezoMEMS.**

Index Terms – **piezoelectricity, microelectromechanical systems (MEMS), thin-films, lead zirconate titanate, humidity barrier, humidity-induced degradation, reliability, lifetime, atomic layer deposition, breakdown**

I. INTRODUCTION

L EAD zirconate titanate (PZT) is a high-performance piezoelectric material widely used for microelectromechanical systems (MEMS)[1], [2].

Piezoelectric thin-films have promising properties for MEMS applications [3], making them attractive for adjustable optics[4]–[6], transducers[7]–[9], FERAM[10]–[12] and energy harvesters[13]–[16]. Ensuring a reliable long-term device operation in realistic and harsh operating conditions is technologically and scientifically important for commercialization of thin-film piezoelectric MEMS (piezoMEMS)[17]–[20]. As such, humidity is a severe ambient stressor[21]–[24]. Operation in humid conditions causes cracking, resistance degradation, excessive leakage, and time-dependent dielectric breakdown (TDDB) considerably faster than for operation under dry conditions[25], [26]. For PZT-based piezoMEMS, early onset of transient leakage currents and excessive Joule-heating, which locally vaporize the stack material, has been well established as one of the main degradation effects[27]–[29]. For devices, such electrothermal breakdown-events (ETB) are irreversible (hard) degradation, and may, in addition to TDDB, cause loss of active electrode area, film delamination, decreased structural integrity of the piezoelectric layer-stack and degraded properties of the piezoelectric[30]. Such degradation are expected to affect the dynamic behavior of devices throughout their lifetime and need to be considered, and particularly important to understand, monitor and mitigate for thin-film piezoMEMS, since their functionality is sensitive to the film-substrate stress transfer.

Applying an adequate humidity barrier is generally imperative for improving the reliability and lifetime of piezoMEMS devices[31]–[33]. However, encapsulating thin-film piezoMEMS-devices is challenging for several reasons: (i); devices contain electromechanically moving parts and require mechanically robust and durable humidity barriers, (ii); covering large complex, structured surfaces with a uniform, pinhole-free and sufficiently thin coating, can be challenging, (iii); the additional encapsulation step may affect the properties of the final device, and (iv); the encapsulation method must be CMOS-compatible with the possibility for wafer-level integration[34], [35]. Several encapsulation techniques have been tested, for example using polymers such as parylene-c[36] or epoxy[37]. For thin-film piezoMEMS-devices, Al_2O_3 is a promising barrier material that can be applied using CMOS-compatible techniques due to its low water vapor transmission

rate, high dielectric strength, and good mechanical strength[32], [38]. Atomic layer deposition (ALD) is a promising deposition technique for applying thin Al_2O_3 humidity barriers as it complies well with point (i)-(iv) and uses low-cost precursors[39].

The lifetime of piezoMEMS-devices is often assessed by direct current (DC) TDDB measurements accelerated by electric fields and elevated temperatures[18], [25], [40]–[43]. DC electrical field reliability relates to the various charge-trapping processes and conduction-mechanisms of the thin-film. The leakage current behavior depends on the doping-type and concentration, the films' defect chemistry, thickness, microstructure as well as the characteristics of the PZT-electrode interface[43]–[49]. However, although DC TDDB measurements are important for analyzing essential processes related to the device lifetime, such tests do not provide insight into to the device's dynamic response during degradation, and additional possible failure modes, specific for a unique device geometry[33], [50]. It is, therefore, of interest to study how degradation affects the dynamic behavior as well as the dielectric properties of factual devices during operation. Furthermore, the rate of humidity-related degradation depends on the relative humidity at the surface of the device, and may thus be shadowed by elevated temperatures, often used for accelerating lifetime tests.

This study assesses the electromechanical, piezoelectric, and dielectric/ferroelectric properties of thin-film PZT-based micromirrors during operation at room temperature in dry and humid conditions. The intention is to investigate the effect of humidity-related degradation, and the use of ALD-deposited Al_2O_3 as a strategy for mitigating such degradation, from the perspective of a factual piezoMEMS device. Micromirrors developed at SINTEF MiNaLab[4], were chosen as a model system for this purpose. Here, the development and use of a compact, retrofittable experimental setup allowed for characterizing essential electrical and dynamic aspects related to the reliability of up to five devices simultaneously under controlled humid operating conditions. A two orders of magnitude improved lifetime using humidity barriers is demonstrated. The origins of device failure in humid conditions and important effects of humidity-related degradation on the dynamic behavior of the micromirrors prior to failure are highlighted and discussed.

II. EXPERIMENTAL

Thin-film piezoelectric micromirrors with a functional layer-stack of $Au/TiW/PZT/LaNiO_3/Pt/Ti/SiO_2/Si$ were fabricated using 1.01 ± 0.02 μm thick Ba-doped $PbZr_{0.4}Ti_{0.6}O_3$ (PZT) films with a 90 % / 10 % mixed (001) / (110)-orientation. The PZT thin-films were deposited onto a 10 nm (001)-oriented $LaNiO_3$ buffer/seed-layer using pulsed laser deposition (Solmates SIP 800) on a 6" platinized silicon-on-insulator wafer[34], [51]. The top electrodes, comprised of 250 nm Au on top of a 10 nm Ti with 10 wt% W adhesion-layer, deposited by DC magnetron sputtering, before device definition. A bake out step of 15 minutes at 200 °C was done before electrode deposition to remove potential water-vapor from the substrate. For the present layer stack, the PZT films had a breakdown strength of 500-550 kV/cm with positive and 450-500 kV/cm with negative
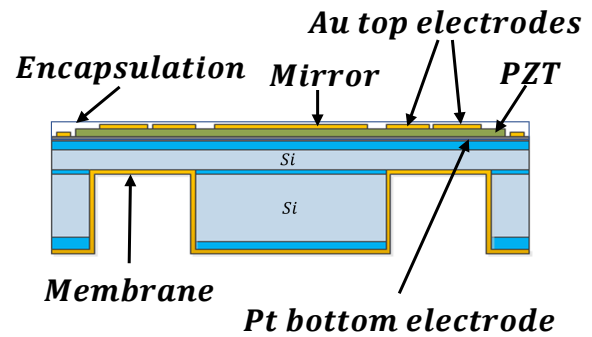

Fig. 1: Side-view schematic of the micromirror. Extended information on device design and functionality can be found in previous work[4], [27].

bias on the top electrode. Positive top electrode bias was, therefore, used in this study. An average stress coefficient of $e_{31,f} = -12.5 \pm 0.3 \left[\frac{C}{m^2}\right]$ was measured by a strain-gauge method [52]. In previous studies [4], it was shown that poling of this particular device geometry resulted in a decreased angular deflection, thus no poling of the devices were done before the experiments. The Al_2O_3 encapsulation was deposited as the last step, using a Beneq TFS-500 ALD reactor maintained at 175 °C, with a working pressure of 3 mbar. The encapsulation had a thickness of 37-40 nm, measured using a J. A. Woolam a-SE spectroscopic ellipsometer. To enable wire-bonding, buffer HF was used to etch through the encapsulation in the middle of the contact pads. The Al_2O_3-layer is expected to add an additional stress of about 400 MPa to the layer-stack [38], [53].

Qualification tests of the pristine devices showed that the PZT films endured more than $1x10^{11}$ degradation-free unipolar fatigue-cycles at 100 kHz and the maximum intended operating voltage of 20 V_{AC} around a 10 V_{DC} offset (0-200 kV/cm) in ambient air of 35 % relative humidity (RH) and 23 °C. At 20 V the devices experience a maximum in-plane strain of 0.093 %. The reader is otherwise directed to the supplementary information for more details.

Fig. 1 shows a cross-section schematic of a final device, diced from the processed 6" wafer. The device comprised a 400 μm thick silicon-disc with a diameter of 3 mm, suspended on an 8 μm thick silicon membrane, structured with backside deep reactive ion etching. The PZT-film was continuous across the 8x8 mm^2 die. Using standard lithography, eight electrodes were defined to form an inner and outer ring on the membrane surrounding the center disc. These were routed by 20 μm wide electrode tracks to bonding pads placed along the outer edge of the die. For the present design, actuating the inner electrodes pushes the centre disc downwards, and actuating the outer electrodes pushes the disc upwards. Here, generating a maximum tip-tilt motion was done by actuating the two inner and two outer electrodes on each opposite sides of the device, as illustrated in Fig. 2 (a). More details on the design and fabrication of the used devices can be found elsewhere[4], [27].

The dynamic behavior was characterized by reflecting a laser off the micromirror's center disc onto a Thorlabs PDP90A position sensitive device (PSD), as shown schematically in Fig. 2 (a). Since the maximum tilt was always less than 1°, the small-angle approximation, $\tan(\theta) \approx \theta$, was used to calculate
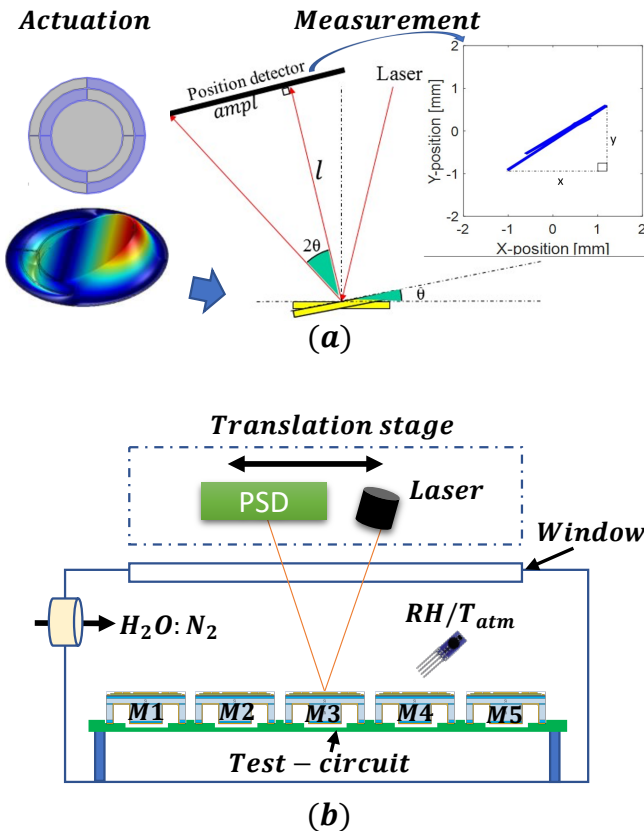
Fig. 2: A schematic of device-actuation and setup for electromechanical characterization is shown in (a). (b) Measurements were carried out in a compact environmental chamber designed for lifetime and reliability testing of piezoMEMS-devices. The ambient humidity was controlled by bubbling N_2 through a DI-water container during testing. The position detector and laser were fixed on a micrometre stage outside the chamber allowing simultaneous characterization of five piezoMEMS-devices in each condition. The setup was retrofitted to an AixACCT TF2000 for leakage, ferroelectric and dielectric characterization of each micromirror.

the amplitude of the angular deflection, θ, based on the recorded x and y laser-trace positions:

$$2\theta \approx tan(2\theta) = \frac{\sqrt{x^2 + y^2}}{l} \qquad (1)$$

This is illustrated to the right in Fig. 2 (a), where $l = 100$ mm is the distance from the device to the PSD, and x and y are the coordinates of the laser trace on the PSD. The x and y coordinates were used to study the evolution of the devices' dynamic response with degradation-time. A maximum angular deflection of 0.6^o was obtained for bare devices at 20 V_{AC} and an excitation frequency of 1.5 kHz, far away from the resonance-frequency of 9 ± 1 kHz. This corresponded to a 15.7 µm distance from the bottom of the tilted center mirror-plane to the neutral plane, during actuation. Throughout the lifetime measurements, the devices were unipolarly cycled using 20 V_{AC}, offset around 10 V_{DC} at 1.5 kHz.

The experimental setup, designed and used for this study, is shown schematically in Fig. 2 (b). For each test condition, five micromirrors were wire-bonded to a polyimide MEMS test circuit and mounted inside a custom-made compact environmental chamber. The humidity inside the chamber was controlled by bubbling N_2 through a DI-water container and flowing the $H_2O:N_2$-mixture through the chamber during the

experiment. Each condition was stabilized prior to, and controlled throughout the measurements, through a LabView-program with a HYT271 humidity sensor. In humid conditions, the ambient was kept at 95% RH at room temperature (23°C). Dry conditions, ~0 % RH, were achieved by flowing dry N_2 through the chamber.

All measurement equipment was kept outside the chamber and contacted to the test circuit using high-temperature wires. Characterizing the dynamic behavior of all five devices was done by mounting the laser and PSD onto an external micrometre stage, moving the laser over each device to be characterized during the experiment. This was enabled by reflecting the laser of the micromirrors through an optical viewport integrated in the environmental chamber. Each device was scanned for 10 seconds before moving to the next micromirror, and the cycle repeated throughout the experiment. Each cycle, scanning across all five micromirrors, had a total duration of 1 minute.

To enable dielectric and ferroelectric characterization, the experimental setup was retrofitted to an AixACCT TF2000 ferroelectric analyzer. The average of 5 polarization-field hysteresis loops was measured at 100 Hz with a large-signal of 20 V_{AC}. For measurements of the permittivity and loss, a small-signal amplitude of 200 mV with a small-signal frequency of 1 kHz was used.

Two failure-conditions were defined: (1) more than $1/e$ loss of angular deflection and (2) TDDB taken as the time when the leakage current increased by two orders of magnitude. The failure probability was calculated using the cumulative distribution function[54], [55]:

$$f(t; \alpha, \beta) = 1 - e^{-\left(\frac{t}{\alpha}\right)^{\beta}} \qquad (2)$$

where β is the shape parameter describing the confidence of the measurement, α the reported time to failure and t the time of operation. Structural characterization was done using optical (Pixelink PL-B623) and scanning-electron microscopy (Quanta 600 FEG SEM). ImageJ image analysis software was used to analyze the post-degradation crater sizes on failed devices.

III. RESULTS AND DISCUSSION

A. Device lifetime and critical flaws
Fig. 3 (a) shows the failure probability-distribution for bare (blue) and encapsulated (red) devices in humid conditions. Applying an Al_2O_3 encapsulation improved the median cycles-to-failure by two orders of magnitude from $4.1x10^7$ [$2.9 - 6x10^7$] to $1.7x10^9$ [$1.4 - 2.3x10^9$]. The confidence intervals are given in the brackets. This corresponds to an increase in MTTF from 8 hours to 314 hours with continuous cycling at maximum specified loading conditions of 200 kV/cm. the corresponding Weibull shapes of $\kappa_{bare} = 1.5$ and $\kappa_{encap} = 2.0$, indicates an increasing failure rate with time, for both bare and encapsulated devices, and will be discussed below.
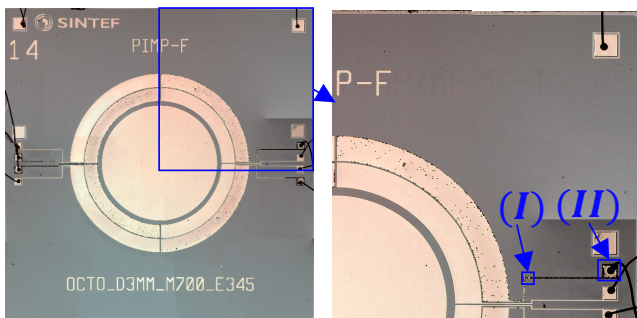
Fig. 3 shows optical images of degraded bare, (b), and encapsulated, (c), devices, after failure. As was also found in previous work[27], all bare devices tested here failed exclusively due to a breach of one of the electrode routings. The loss of electrical connection to the actuation membrane resulted
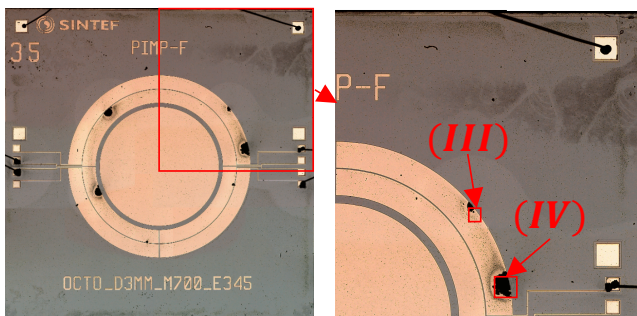
(a)
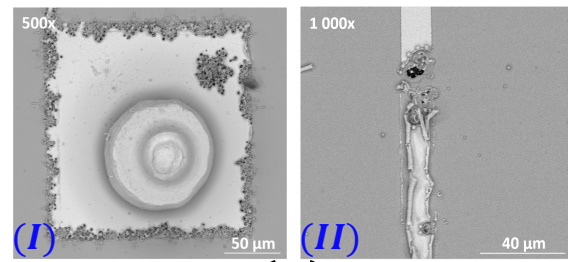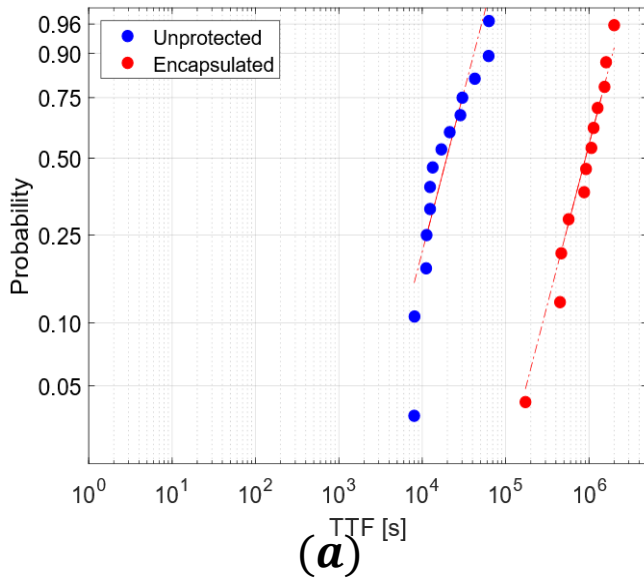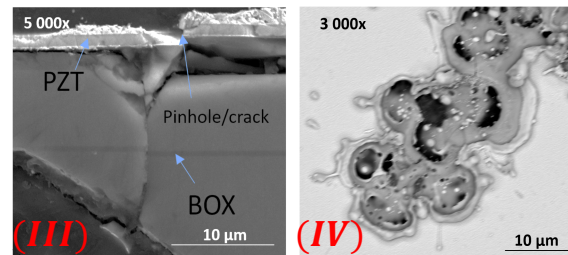
(b)

(c)

Fig. 3: Failure probability as a function of time is shown in (a), and optical images of bare and encapsulated devices, post-failure, are shown in (b) and (c). A close-up of a region of interest is shown to the right in (b) and (c) and analyzed further by SEM in Fig. 4. During degradation, ETB-events with an average post-failure crater size of $150 \pm 40\ \mu m^2$ appeared more frequently along the electrode edges for bare devices than for encapsulated. In comparison, the encapsulated devices displayed similar degradation at localized points, with an average post-failure crater size of $2.7x10^4 \pm 1.5x10^4\ \mu m^2$.

in a power cut and therefore a drop in angular deflection. This contrasts with a gradual loss of angular deflection driven by e.g., polarization or mechanical fatigue. The failure was predominantly driven by ETB-events on the active top electrode areas (anode), eventually causing a connection breach due to material melting/evaporation, and/or film delamination.

(a)

(b)

Fig. 4: Post-failure SEM-images of bare, (a) and encapsulated (b) devices from points (I)-(IV) indicated in Fig. 3. Smaller craters more frequently located along the electrode edges than on the membrane surface was found on bare devices, compared to encapsulated devices. The latter displayed, fewer, larger, and more localized failure-points, containing large cracks all the way through the device-layer as shown in (III) and (IV).

Examples of such ETB-events and routing breaches, post-failure, are shown for bare devices in the optical images of Fig. 3 (b). SEM images of the indicated points, (I) and (II), are shown in Fig. 4 (a). Post-failure, the ETB-craters of the bare devices covered an average $150 \pm 40\ \mu m^2$ of the electrode surface area, with most of the craters appearing along the electrode edges. From elemental mapping of post-failed devices (not shown here), residuals of Si, PZT, Pt, and Au were found both inside the post-failure craters and scattered across the electrode surface, consistent with degradation observed in previous work[24], [27] and with other literature reports[24]. For the present device design the critical flaw was located at the 20 μm wide electrode routings, which make up about 1/3 of the total electrode circumference (approx. 11 mm). Since the width of the routings is comparable in size to the ETB craters, they are particularly prone to failure during degradation, as exemplified in (II) of Fig. 4 (a).

For the encapsulated devices, degradation was manifested as an intermixing of amplitude-loss and TDDB. This is also reflected in $\kappa_{encap} > \kappa_{bare}$, and devices failing more rapidly with time after the initial onset, since more degradation-mechanisms come into play. As indicated by point (III) and (IV) of Fig. 3 (b) and Fig. 4 (b), the more localized and considerably more extensive ETB craters had average crater size of $26\,000 \pm 15\,000\ \mu m^2$. They appeared close to the wire-bonding pads, at localized points along the electrode edges, and on top of the electrode-surface. For the latter, sputtered particles in the piezoelectric was found to correlate directly with localized ETB events (see supplementary information). This indicates that various defects, such as large PZT particles deposited during the PLD process, microcracks from the

process of wire-bonding or small nonuniformities in encapsulation coverage at step-edges etc., are vulnerable points on the encapsulated device, contributing to encapsulation breach and degradation onset. Additionally, large stress/strain-gradients, particularly at the electrode edges, may also contribute to such cracking and encapsulation-breach when the electromechanical deflection is high, here up to 15 µm at a 20 V bias. After an encapsulation-breach, degradation in the form of ETB events and further cracking can proceed and spread from its initial site along the device for an extended period, without necessarily inducing immediate device failure. This enlarges the post-failure crater-sizes with time and induce considerable damage to the membrane structure, as well as loss of top electrode-area on encapsulated devices as exemplified in (III)-(IV) of Fig. 4 (b) (see the supplementary information for more details).

B. Leakage transients and effect on dynamic behavior

The evolution of leakage together with the dynamic behavior was recorded throughout the degradation and is exemplified in Fig. 5 (a). The blue and black curves show typically encountered leakages as function of degradation time for a bare device and for an encapsulated device, respectively. TDDB is indicated by the dotted lines and relate the leakage-measurements in Fig. 5 (a) with the corresponding deflection measurements in Fig. 5 (b). A bare device operated in dry ambient is included for reference (green curve). From the leakage vs. time measurements in humid conditions, the degradation displayed traits similar to that of typical TDDB in dry conditions, but on a much reduced timescale. Leakage transients were observed in humid atmosphere after about $6x10^3$ s ($\sim 9x10^6$ cycles) for bare and after about $8x10^4$ s ($\sim 1x10^8$ cycles) for encapsulated devices. In comparison, few or no transients, and no dielectric breakdown were recorded within the experimental timeframe in dry conditions, as shown by the green curve in Fig. 5 (a).

Several mechanisms can contribute to ETB, depending on the applied field, ambient humidity and the particular layer-stack being tested. At low humidity levels, the accumulation of oxygen vacancies near the cathode region, electron injection and Schottky-barrier lowering are well-known mechanisms causing resistance degradation[47], [48], [56]–[58]. Under moderately temperature- and field-accelerated conditions, electrical degradation and dielectric breakdown typically occurs over a period of 10^5-10^6 s.

In high humidity, the presence of surface water can catalyze metal electromigration of e.g. Ag, Cu or Pd from the anode to the cathode side, creating dendrites which upon reaching a critical thickness induce ETB[30], [59]. The reduction of PbO and the formation of Pb-filaments is another proposed mechanism, but has, to the author's knowledge, not yet been observed. For the RH and layer-stack used in the current study, the data is consistent with water-electrolysis: $H_2O(g) \rightarrow H_2(g) + O_2(g)$ and electrochemical compression of gas trapped at the piezoelectric thin film/electrode interfaces, as the driving mechanism[24]. Degradation occurs through cracking, delamination, and failure by ETB, caused by dielectric breakdown through humidified air separating the top and bottom electrodes in cracks and voids. The more frequent
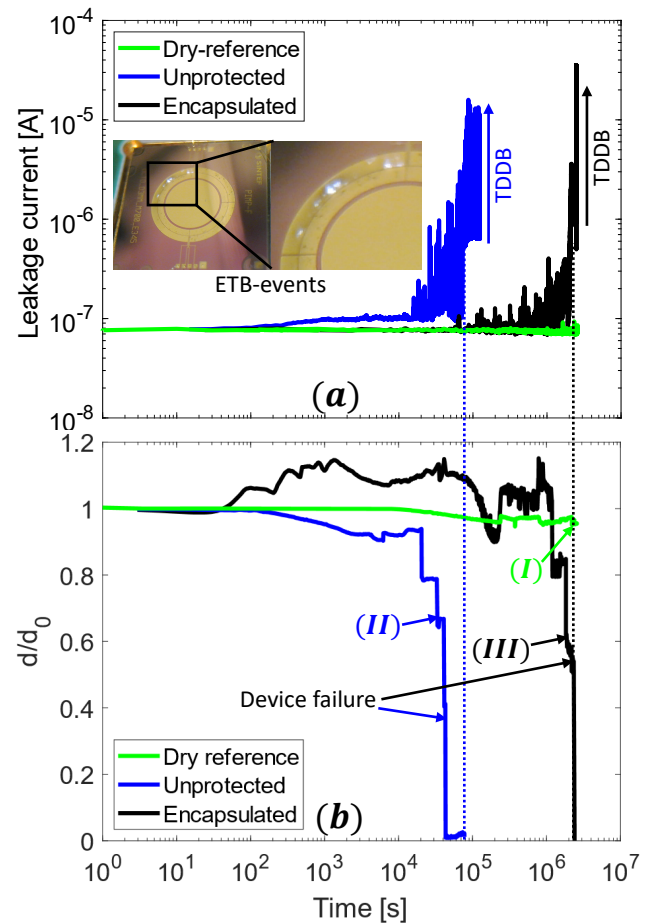

Fig. 5: Degradation during operation at 1.5 kHz as a function of time for bare (blue) and encapsulated (black) devices in humid conditions. The green curve shows a typical bare device in dry ambient for comparison. The measured leakage is shown in (a) and the relative angular deflection in (b). The inset shows recorded in-situ ETB-events, manifested as arcing, after about 3x10⁴ s. Pre-failure degradation was generally associated with leakage-transients and ETB, severely affecting both the angular deflection amplitude and the dynamic response of both bare and encapsulated devices, as illustrated by point (I)-(III) and further illustrated in Fig. 6.

appearance of ETB along the edges of the active positrodes is consistent with this model, as the edges offer easier pathways for transport and trapping of water molecules underneath the electrode. It is also suggested that a higher electrochemical activity of oxidized TiW adhesion-layer, could locally increase the evolution of $H^+/O_2(g)$[60]–[66].

After the onset, the number of leakage transients increased with operation time, on both bare and encapsulated devices, consistent with the literature[67]. In contrast to degradation in dry conditions, transients in humid conditions arise from an interplay between cracking and water adsorption/desorption dynamics creating temporary current transients along the surface and in cracks/voids, as the device start to behave as an electrochemical cell[68]–[70]. This is supported by in-situ recordings of arcing-events showing a direct connection between transients and ETB, as exemplified for bare devices after about $3x10^4$ s of degradation in the inset images of Fig. 5 (a). Hence for humid conditions, the onset of transients indicates the start of hard degradation-events and the beginning of device failure. Thus, only partial recovery of thin-film devices can be achieved by post-degradation annealing[28],
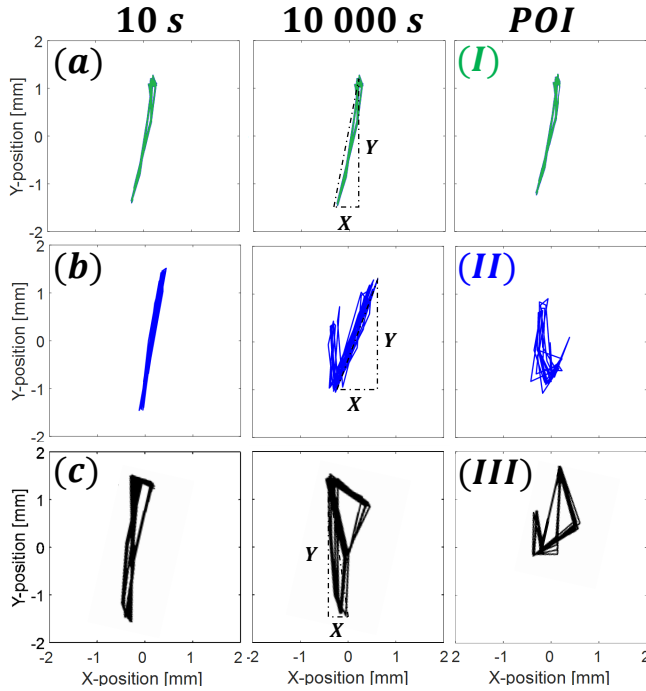
Fig. 6: X/Y laser-traces at the indicated points of Fig. 5 (b). Recorded responses of bare devices (blue) are shown in (a), encapsulated devices (black) in (b) in humid conditions. The dry reference is shown in (c). The X/Y positions indicate the points used for calculating the angular deflection-amplitude.

[71], and reduced reliability should be expected upon continued usage in humid as well as in dry conditions.

Angular deflection amplitude relative to the device's initial deflection amplitude is plotted as a function of degradation time for bare (blue curve) and encapsulated (black curve) devices in humid conditions in Fig. 5 (b). A measurement of a bare device in dry conditions (green curve) is included for reference. (I), (II) and (III) relates to points for which the laser-trace has been extracted, and are shown in Fig. 6.

In dry conditions, the degradation rate followed a logarithmic decay, characteristic for polarization- and electrical field-driven fatigue processes[72]–[75]:

$$d = d_0 - R\log(t) \qquad (3)$$

Here d_0 is the initial deflection amplitude, R the rate of change, and t the time of operation in seconds. The decrease in angular deflection was $R_{bare} = 0.03 \pm 0.01$ %/decade and $R_{encap} = 0.11 \pm 0.05$ %/dec for the bare and encapsulated devices, respectively. Apart from the small amplitude loss with time, presumably from general fatigue-related mechanisms[75], devices operated with a stable linear response and no device failure for more than $5x10^9$ unipolar cycles at 1.5 kHz (38 days) in dry conditions.

In humid conditions, the dynamic behavior of both bare and encapsulated devices differed significantly from the behavior at dry conditions after 10^2 s. Routing-breaches were manifested as four sudden losses (drops) of angular deflection, corresponding to each of the four actuated electrodes, as shown in Fig. 5 (b). The electrode loosing electrical connection could be inferred by the change of the direction of the tip-tilt motion

from the X-Y laser traces. The probability of a certain routing to fail first, however, could not be identified. Complete device failure occurred at the last routing-breach, as indicated by the arrows in Fig. 5 (b).

ETB, cracking, and electrode delamination significantly altered the dynamic device behavior before failure. The recorded X- and Y-traces of the bare (blue) and encapsulated (black) devices, as shown in Fig. 6 (b)-(c), illustrates changes in the tip-tilt motion encountered during degradation. (I)-(III) shows the X/Y laser-traces after 10 s, 10 000 s, and at points of interest from Fig. 5 (b).

In general, distortions in the dynamic behavior were manifested as additional tilt-twist motions gradually deviating from the linear tilt-motion otherwise maintained in dry conditions. The SEM-analysis in Fig. 3 (b), indicates that these distortions are due to cracking, partial loss of electrode area, delamination, and de-clamping, changing the amplitude and distributed forces acting on the membrane. As exemplified in the 10 s column of Fig. 6 (a)-(c), minor distortions could be detected in a number of the pristine devices. Since thin-film devices work by the film-substrate stress-transfer making them sensitive to the in-plane circumstances of the film, minor distortions are assumed to stem from processing-related variations across the wafer. This includes small variations in film thickness, roughness, texture, or substrate clamping, and becoming more prominent for geometries using relatively large electrodes (here ~1.2 mm²). It is notable that, in humid conditions, the characteristic minor distortion of the tip-tilt motion evolve to become a major distortion as the degradation proceeds. This contrasts to operation in dry conditions, where the magnitude of the distortion remains throughout the experimental time, as is particularly clear when comparing the X/Y-scans after 10 and 10 000 s operation in Fig. 6 (a) and (c). This supports the findings and humidity related degradation mechanisms discussed above, i.e. the initiation and spreading of the degradation is related to the processing parameters. With time, degradation translates into relatively large macroscopic changes in the electromechanical response, including geometric nonlinearities, transverse resonance-shifts, angular deflection hysteresis, nonlinear normal modes, and bifurcations, prior to TDDB or loss of considerable deflection amplitude[76]–[80].

It is also plausible that the in-plane piezoelectric stresses combined with the residual stress generate cracks that initiate degradation, as both can be up to tens to hundreds of MPa[81]–[84]. As shown in the supplementary information, the PZT films used in this study were, based on wafer-bending measurements[85], [86], found to hold a tensile residual stress

Tab. 1: Characteristic values for the bare and encapsulated devices. The 95 % confidence intervals are given in the brackets for the MTTF-measurements.

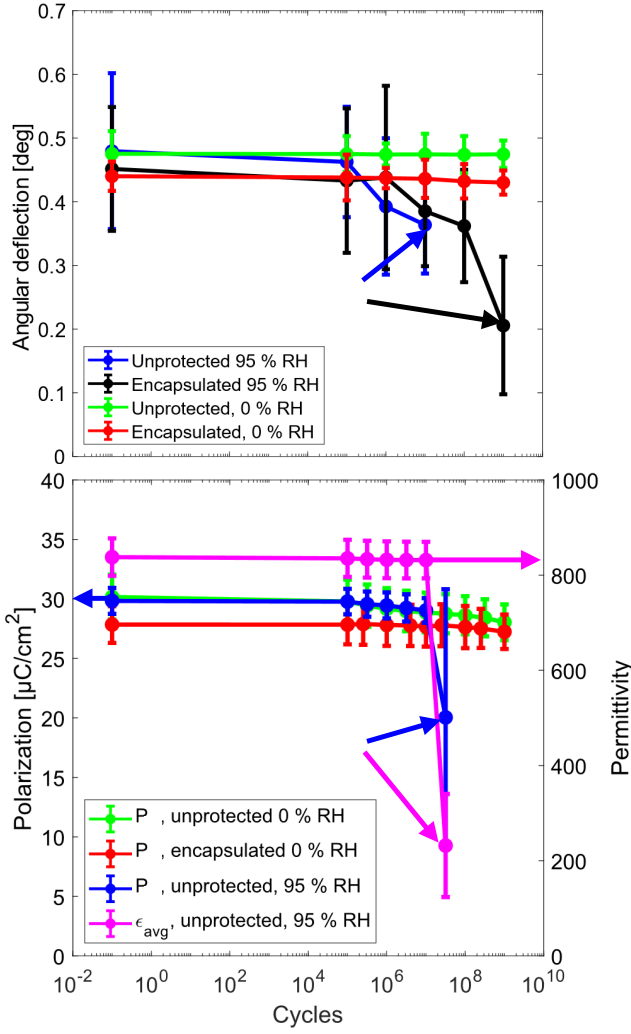| Parameter	Bare	Encapsulated
A_{ETB} [μm²] 95 % RH	150 ± 40	$27\,000 \pm 15\,000$
$P_{200\,kV/cm,\,init.}$ [μC/cm²]	30.6 ± 1.0	27.3 ± 0.4
$\varepsilon_{0\,V,\,initial}$	1218 ± 53	1066 ± 61
$d_{200\,kV/cm,\,initial}$ [°]	0.48 ± 0.06	0.45 ± 0.08
R_d 0% RH [%/dec]	-0.03 ± 0.01	-0.11 ± 0.05
R_{P_M} 0% RH [%/dec]	-0.45 ± 0.17	-0.67 ± 0.14
R_ε 0% RH [%/dec]	-0.001 ± 0.001	-0.010 ± 0.005
MTTF [s] 95 % RH	$\alpha = 2.7x10^4/\kappa = 1.5$	$\alpha = 1.1x10^6/\kappa = 2.0$
	$[1.9x10^4 - 4.0x10^4]$	$[0.9x10^6 - 1.5x10^6]$
Failure type	Deflection loss	Deflection loss/TDDB

Fig. 7: Average angular deflection as a function of actuation cycles for bare dry (green), encapsulated dry (red), bare humid (blue) and encapsulated humid are shown in (a). The corresponding average polarization and permittivity (magenta) are shown in (b). The latter is here only plotted for unprotected devices in humid conditions for illustration purposes, noting that similar behavior was measured for encapsulated devices. P-E and ε-E loops can be found in the supplementary information. Pristine encapsulated devices showed a 6, 10 and 12 % decreased initial deflection amplitude, polarization and permittivity compared to pristine bare devices. Degradation characteristic for dry conditions was generally consistent with a polarization-fatigue model. In humid conditions, degradation manifested itself as a rapid loss of angular deflection after the onset of ETB. The onset of ETB started after $6.1 \pm 4.2x10^3$ s ($9.2 \pm 6.3x10^6$ cycles) for bare devices and after $7.9 \pm 3.8x10^4$ s ($1.2 \pm 0.6x10^8$ cycles) for encapsulated devices. The large sample-to-sample variations are reflected in the large standard deviations. Device failure due to the breach of an electrode routing is indicated by a drop in polarization, permittivity, and angular deflection.

of $\sigma_R = 270 \pm 70$ MPa post processing. At 200 kV/cm, the in-plane piezoelectric stress, $\sigma_X = -e_{31,f}E_Z(t)$ is 240 MPa tensile, which when added to the residual stress, surpass the critical stress of PZT (~550 MPa) during operation[74], [87]–[89]. Improved reliability in humid conditions may thus be achieved by reducing the number of post-processing defects, reduce the residual film stress, improve the mechanical limits of the piezoelectric and improve the mechanical strength of the humidity barrier[90].

C. Ferroelectric, dielectric, and piezoelectric properties

For ferroelectric and dielectric measurements, the cycling of selected samples was interrupted three times per decade to measure polarization-field (P-E) and permittivity-field (ε-E) hysteresis loops in both dry and humid conditions. The average maximum polarization (P_M), average permittivity (ε_{avg}), and angular deflection (d_{avg}) of five micromirrors as a function of degradation-cycles in dry and humid conditions are shown for bare and encapsulated devices in Fig. 7 (a) and (b). Device failure in humid operating conditions are indicated by the colored arrows. Typical P-E, ε-E and d-E hysteresis-loops can be found in the supplementary information, and corresponding average values are summarized in Tab. 1. For the pristine bare devices $d_{max} = 0.48 \pm 0.06^\circ$, $P_M = 30.6 \pm 1.0$ µC/cm^2, $E_C^+ = 27.5 \pm 1.2$ kV/cm, $\varepsilon_{0\,V} = 1218 \pm 53$ and $\tan(\delta) = 0.08 \pm 0.03$ respectively. For the encapsulated devices, $d_{max} = 0.45 \pm 0.08^\circ$, $P_{max} = 27.3 \pm 0.4$ µC/cm^2, $\varepsilon_{0\,V} = 1066 \pm 61$. This corresponds to a reduction of about 6, 11 and 12 % compared to the properties of the bare devices. Since $e_{31,f} \propto P\varepsilon$, reduced piezoelectric properties fits well with a reduction in P and ε and are ascribed to the additional encapsulation-step. Though not distinguished here, factors such the incorporation of protonic defects into PZT during the ALD process[91]–[93] or thermal hysteresis[94], may impede the piezoelectric response and decrease the overall reliability of piezoMEMS-devices. Furthermore, while degradation-rates of $R_{P_M} = -0.45$ %/dec, $R_{\varepsilon_{avg}} = -0.009$ %/dec and $R_d = -0.03$ %/dec for the bare devices, the degradation-rates increased to $R_{P_M} = -0.67$ %/dec, $R_{\varepsilon_{avg}} = -0.010$ %/dec and $R_d = -0.11$ %/dec for the encapsulated devices. These results correlate well with a polarization-fatigue driven model; the extrinsic contributions to the piezoelectric effect degrades by the immobilization of domain walls in which the accumulation of oxygen vacancies near the cathode region is particularly important[43], [44], [95], [96]. Although the devices will degrade electrically with time, eventually resulting in TDDB also in dry conditions, the present results indicate that the devices should be able to survive for realistic product lifetimes without failure [97]–[100].

In humid conditions, the measured decrease in ferroelectric, dielectric and piezoelectric properties with time were found to be directly connected to the loss of electrode area due to ETB, as detailed in the supplementary information. When corrected for, no significant degradation exceeding the dry-equivalent behavior was measured. This correlates well with degradation driven by water electrolysis, which is a DC phenomenon, and will "freeze-out" in the high AC frequency range (>100 Hz).

IV. CONCLUSIONS

In conclusion, the median time-to-failure of thin-film PZT-based micromirrors increased from $2.7x10^4$ s [$1.9x10^4 - 4.0x10^4$ s] s to $1.1x10^6$ s [$0.9x10^6 - 1.5x10^6$ s] under continuous unipolar operation at 0-200 kV/cm in 95 % relative humidity, by using a 40 nm thick Al_2O_3 barrier-layer deposited by atomic-layer deposition. Using a relatively small number of samples, important effects of humidity-related degradation on reliability and dynamic behavior of factual piezoMEMS devices have been highlighted. In the pristine state,

encapsulated devices displayed a reduction in maximum polarization, permittivity, and initial angular deflection of about 10, 12 and 6 %, relative to bare devices, accompanied with an increased fatigue-rate compared to the bare devices in dry conditions. The reduction in initial performance was ascribed to effects related to the additional encapsulation step.

Consistent with degradation-mechanisms proposed in previous work, the early onset of leakage-transients connected with electrothermal breakdown-events, preceded that of time-dependent dielectric breakdown, and was found to drive device degradation in humid conditions. Post-failure craters appeared more frequently along the edges of the biased top electrode, and at sites containing processing-related defects, including cracks, sputtered particles or nonuniform coverage of the humidity barrier-layer. For the bare devices, the size of each post-failure crater was 150 ± 40 μm^2 while for the encapsulated devices, the size of each crater was $27\,000 \pm 15\,000$ μm^2. This was consistent with degradation initiated at and spreading from a singularity of various processing-related defects. For all bare devices, the electrode routings were identified as the critical flaw, resulting in failure by the loss of angular deflection. For the encapsulated devices, on the other hand, failure was due to a combination of time-dependent dielectric breakdown, routing breaches and loss of angular deflection.

In all cases of degradation, cracks, delaminated electrodes, and craters from electrothermal breakdown-events severely affected the devices' dynamic behavior, and reduced device-reliability before failure. Signature tip-tilt motions, presumably originating from minor processing related defects, intensified as degradation preceded in humid conditions, as opposed to remaining stable in dry conditions. Apart from the loss of electrode area, however, humidity induced degradation was not found to significantly alter the polarizability, permittivity, or loss.

V.   REFERENCES

[1]   S. Trolier-McKinstry, S. Zhang, A. J. Bell, and X. Tan, "High-Performance Piezoelectric Crystals, Ceramics, and Films," *Annu. Rev. Mater. Res.*, vol. 48, no. 1, pp. 191–217, 2018, doi: 10.1146/annurev-matsci-070616-124023.

[2]   C.-B. Eom and S. Trolier-McKinstry, "Thin-film piezoelectric MEMS," *MRS Bull.*, vol. 37, no. 11, pp. 1007–1017, 2012, doi: 10.1557/mrs.2012.273.

[3]   Yole Développement, "Status of the MEMS Industry 2019 Market and technology Report," 2019.

[4]   T. Bakke, A. Vogl, O. Zero, F. Tyholdt, I. R. Johansen, and D. Wang, "A novel ultra-planar, long-stroke and low-voltage piezoelectric micromirror," *J. Micromechanics Microengineering*, vol. 20, no. 6, pp. 1–7, 2010, doi: 10.1088/0960-1317/20/6/064010.

[5]   V. Cotroneo, W. N. Davis, P. B. Reid, D. A. Schwartz, S. Trolier-McKinstry, and R. H. T. Wilke, "Adjustable grazing incidence x-ray optics: measurement of actuator influence functions and comparison with modeling," in *Optics for EUV, X-Ray, and Gamma-Ray Astronomy V*, 2011, vol. 8147, p. 81471R, doi: 10.1117/12.895475.

[6]   "Polewall Home - Polewall." [Online]. Available: https://www.polewall.com/. [Accessed: 06-Jun-2019].

[7]   Y. Qiu *et al.*, "Piezoelectric micromachined ultrasound transducer (PMUT) arrays for integrated sensing, actuation and imaging," *Sensors (Switzerland)*, vol. 15, no. 4. Multidisciplinary Digital Publishing Institute (MDPI), pp. 8020–8041, 03-Apr-2015, doi: 10.3390/s150408020.

[8]   H. S. Choi, J. L. Ding, A. Bandyopadhyay, M. J. Anderson, and S. Bose, "Characterization and modeling of a piezoelectric micromachined ultrasonic transducer with a very large length/width aspect ratio," *J. Micromechanics Microengineering*, vol. 18, no. 2,

p. 025037, 2008, doi: 10.1088/0960-1317/18/2/025037.

[9]   Y. Kusano *et al.*, "Effects of DC Bias Tuning on Air-Coupled PZT Piezoelectric Micromachined Ultrasonic Transducers," *J. Microelectromechanical Syst.*, vol. 27, no. 2, pp. 296–304, Apr. 2018, doi: 10.1109/JMEMS.2018.2797684.

[10]   M. Pešić and U. Schroeder, "Antiferroelectric One Transistor/One Capacitor Memory Cell," in *Ferroelectricity in Doped Hafnium Oxide: Materials, Properties and Devices*, Woodhead Publishing, 2019, pp. 425–435.

[11]   A. Chen, "A review of emerging non-volatile memory (NVM) technologies and applications," *Solid. State. Electron.*, vol. 125, pp. 25–38, 2016, doi: 10.1016/j.sse.2016.07.006.

[12]   B. Dieny, R. Sousa, G. Prenat, L. Prejbeanu, and O. Redon, "Hybrid CMOS/magnetic memories (MRAMs) and logic circuits," in *Emerging Non-Volatile Memories*, vol. 9781489975, 2014, pp. 37–101.

[13]   M. D. Nguyen, E. Houwman, M. Dekkers, D. Schlom, and G. Rijnders, "Research Update: Enhancement of figure of merit for energy-harvesters based on free-standing epitaxial Pb(Zr0.52Ti0.48)0.99Nb0.01O3 thin-film cantilevers," *APL Mater.*, vol. 5, no. 7, pp. 0–7, 2017, doi: 10.1063/1.4978273.

[14]   H. Elahi, M. Eugeni, and P. Gaudenzi, "A Review on Mechanisms for Piezoelectric-Based Energy Harvesters," *Energies*, vol. 11, no. 7, p. 1850, 2018, doi: 10.3390/en11071850.

[15]   M. El-hami *et al.*, "Design and fabrication of a new vibration-based electromechanical power generator," *Sensors Actuators, A Phys.*, vol. 92, no. 1–3, pp. 335–342, Aug. 2001, doi: 10.1016/S0924-4247(01)00569-6.

[16]   Q. Shi, T. Wang, and C. Lee, "MEMS Based Broadband Piezoelectric Ultrasonic Energy Harvester (PUEH) for Enabling Self-Powered Implantable Biomedical Devices," *Sci. Rep.*, vol. 6, no. 1, p. 24946, Jul. 2016, doi: 10.1038/srep24946.

[17]   C. Dagdeviren *et al.*, "Conformal piezoelectric systems for clinical and experimental characterization of soft tissue biomechanics," *Nat. Mater.*, vol. 14, no. 7, pp. 728–736, Jul. 2015, doi: 10.1038/nmat4289.

[18]   A. E. Islam, "Current Status of Reliability in Extended and beyond CMOS Devices," *IEEE Trans. Device Mater. Reliab.*, vol. 16, no. 4, pp. 647–666, Dec. 2016, doi: 10.1109/TDMR.2014.2348940.

[19]   J. F. Ihlefeld *et al.*, "Room-temperature voltage tunable phonon thermal conductivity via reconfigurable interfaces in ferroelectric thin films," *Nano Lett.*, vol. 15, no. 3, pp. 1791–1795, Mar. 2015, doi: 10.1021/nl504505t.

[20]   "the problem - PETMEM-H2020." [Online]. Available: https://www.petmem.eu/. [Accessed: 06-Jun-2019].

[21]   J. D. Baniecki, J. S. Cross, M. Tsukada, and J. Watanabe, "H2O vapor-induced leakage degradation of Pb(Zr,Ti)O3 thin-film capacitors with Pt and IrO2 electrodes," *Appl. Phys. Lett.*, vol. 81, no. 20, pp. 3837–3839, 2002, doi: 10.1063/1.1519359.

[22]   J. M. Polfus, T. S. Bjørheim, T. Norby, and R. Bredesen, "Surface defect chemistry of Y-substituted and hydrated BaZrO3 with subsurface space-charge regions," *J. Mater. Chem. A*, vol. 4, no. 19, pp. 7437–7444, 2016, doi: 10.1039/c6ta02067d.

[23]   M. B. Starr and X. Wang, "Coupling of piezoelectric effect with electrochemical processes," *Nano Energy*, vol. 14, pp. 296–311, 2014, doi: 10.1016/j.nanoen.2015.01.035.

[24]   R. P. Dahl-Hansen *et al.*, "Electrochemically driven degradation of chemical solution deposited ferroelectric thin-films in humid ambient," *J. Appl. Phys.*, vol. 127, no. 24, p. 244101, Jun. 2020, doi: 10.1063/5.0003989.

[25]   D. Zheng, J. Swingler, and P. M. Weaver, "Electrical conduction mechanisms in piezoelectric ceramics under harsh operating conditions," *Sensors Actuators, A Phys.*, vol. 167, no. 1, pp. 19–24, 2011, doi: 10.1016/j.sna.2010.10.022.

[26]   M. Shoaib, N. H. Hamid, A. F. Malik, N. B. Zain Ali, and M. Tariq Jan, "A Review on Key Issues and Challenges in Devices Level MEMS Testing," *J. Sensors*, vol. 2016, pp. 1–14, 2016, doi: 10.1155/2016/1639805.

[27]   R. P. Dahl-Hansen, T. Tybell, and F. Tyholdt, "Performance and reliability of PZT-based piezoelectric micromirrors operated in realistic environments," in *2018 IEEE ISAF-FMA-AMF-AMEC-PFM Joint Conference, IFAAP 2018*, 2018, pp. 1–4, doi: 10.1109/ISAF.2018.8463243.

[28]   J. Wang, C. Salm, E. Houwman, M. Nguyen, and J. Schmitz, "Humidity and polarity influence on MIM PZT capacitor

degradation and breakdown," *Proc. 2016 IEEE Int. Integr. Reliab. Work. IIRW 2016*, vol. 0, pp. 65–68, 2017, doi: 10.1109/IIRW.2016.7904903.

[29] I. P. Lipscomb, P. M. Weaver, J. Swingler, and J. W. McBride, "Micro-computer tomography-An aid in the investigation of structural changes in lead zirconate titanate ceramics after temperature-humidity bias testing," *J. Electroceramics*, vol. 23, no. 1, pp. 72–75, 2009, doi: 10.1007/s10832-008-9537-8.

[30] D. Zheng, M. Luo, and J. Swingler, "Multi-breakdown model for explaining the formation and growth of black spots in PZT capacitor under DC bias," *Sensors Actuators, A Phys.*, vol. 241, pp. 197–202, 2016, doi: 10.1016/j.sna.2016.02.024.

[31] H. A. C. Tilmans *et al.*, "MEMS packaging and reliability: An undividable couple," *Microelectron. Reliab.*, vol. 52, no. 9–10, pp. 2228–2234, 2012, doi: 10.1016/j.microrel.2012.06.029.

[32] Y. C. Han, E. Kim, W. Kim, H. G. Im, B. S. Bae, and K. C. Choi, "A flexible moisture barrier comprised of a SiO2-embedded organic-inorganic hybrid nanocomposite and Al2O3for thin-film encapsulation of OLEDs," *Org. Electron. physics, Mater. Appl.*, vol. 14, no. 6, pp. 1435–1440, 2013, doi: 10.1016/j.orgel.2013.03.008.

[33] P. Rafiee, G. Khatibi, and M. Zehetbauer, "A review of the most important failure, reliability and nonlinearity aspects in the development of microelectromechanical systems (MEMS)," *Microelectron. Int.*, vol. 34, no. 1, pp. 9–21, 2017, doi: 10.1108/MI-03-2015-0026.

[34] M. Dekkers *et al.*, "Wafer level integration of epitaxial piezoelectric thin films for novel NEMS, MEMS and MOEMS applications," *Adv. Mater. - TechConnect Briefs 2017*, vol. 4, no. building 46, pp. 5–8, 2017.

[35] E. Bouyssou, R. Jérisian, N. Cézac, P. Leduc, G. Guégan, and C. Anceau, "Wafer level reliability and leakage current modeling of PZT capacitors," in *Materials Science and Engineering B: Solid-State Materials for Advanced Technology*, 2005, vol. 118, no. 1–3, pp. 28–33, doi: 10.1016/j.mseb.2004.12.056.

[36] J. Choi *et al.*, "Thin-film piezoelectric and high-aspect ratio polymer leg mechanisms for millimeter-scale robotics," doi: 10.1007/s41315-017-0017-7.

[37] J. Rho, S. J. Kim, W. Heo, N. E. Lee, H. S. Lee, and J. H. Ahn, "PbZrxTi1-xO3 ferroelectric thin-film capacitors for flexible nonvolatile memory applications," *IEEE Electron Device Lett.*, vol. 31, no. 9, pp. 1017–1019, Sep. 2010, doi: 10.1109/LED.2010.2053344.

[38] D. C. Miller *et al.*, "Thermo-mechanical properties of alumina films created using the atomic layer deposition technique," *Sensors Actuators, A Phys.*, vol. 164, no. 1–2, pp. 58–67, Nov. 2010, doi: 10.1016/j.sna.2010.09.018.

[39] J. Sarkar, "Chapter 2 - Sputtering and Thin Film Deposition," in *Sputtering Materials for VLSI and Thin Film Devices*, J. Sarkar, Ed. Boston: William Andrew Publishing, 2014, pp. 93–170.

[40] W. Zhu, B. Akkopru-Akgun, and S. Trolier-McKinstry, "Highly accelerated lifetime testing of potassium sodium niobate thin films," *Appl. Phys. Lett.*, vol. 111, no. 21, p. 212903, Nov. 2017, doi: 10.1063/1.4995618.

[41] S. W. Ko *et al.*, "Improvement of reliability and dielectric breakdown strength of Nb-doped lead zirconate titanate films via microstructure control of seed," *J. Am. Ceram. Soc.*, vol. 102, no. 3, pp. 1211–1217, Mar. 2019, doi: 10.1111/jace.15940.

[42] P. Pertsch, B. Broich, R. Block, S. Richter, and E. Hennig, "Development of highly reliable piezo multilayer actuators and lifetime tests under DC and AC operating conditions," 2010.

[43] B. Akkopru-Akgun, W. Zhu, C. A. Randall, M. T. Lanagan, and S. Trolier-Mckinstry, "Polarity dependent DC resistance degradation and electrical breakdown in Nb doped PZT films," *APL Mater.*, vol. 7, no. 12, p. 120901, Dec. 2019, doi: 10.1063/1.5115391.

[44] D. M. Marincel *et al.*, "A-site stoichiometry and piezoelectric response in thin film PbZr1-xTixO3," *J. Appl. Phys.*, vol. 117, no. 20, 2015, doi: 10.1063/1.4921869.

[45] W. Zhu *et al.*, "Influence of PbO content on the dielectric failure of Nb-doped {100}-oriented lead zirconate titanate films," *J. Am. Ceram. Soc.*, vol. 102, no. 4, pp. 1734–1740, 2018, doi: 10.1111/jace.16000.

[46] B. Akkopru-Akgun, W. Zhu, M. T. Lanagan, and S. Trolier-McKinstry, "The effect of imprint on remanent piezoelectric properties and ferroelectric aging of PbZr 0.52 Ti 0.48 O 3 thin films," *J. Am. Ceram. Soc.*, no. August 2018, pp. 1–14, 2019, doi: 10.1111/jace.16367.

[47] H. N. Al-Shareef and D. Dimos, "Leakage and Reliability Characteristics of Lead Zirconate Titanate Thin-Film Capacitors," *J. Am. Ceram. Soc.*, vol. 80, no. 12, pp. 3127–3132, Jan. 2005, doi: 10.1111/j.1151-2916.1997.tb03240.x.

[48] L. M. Garten, M. Hagiwara, S. W. Ko, and S. Trolier-McKinstry, "Physically based DC lifetime model for lead zirconate titanate films," *Appl. Phys. Lett.*, vol. 111, no. 12, p. 122903, Sep. 2017, doi: 10.1063/1.4994992.

[49] K. Niwa, Y. Kotaka, M. Tomotani, H. Ashida, Y. Goto, and S. Otani, "Interface between electrode and PZT memory device," *Acta Mater.*, vol. 48, no. 18–19, pp. 4755–4762, 2000, doi: 10.1016/S1359-6454(00)00268-8.

[50] M. K. Mishra, V. Dubey, P. M. Mishra, and I. Khan, "MEMS Technology: A Review," *J. Eng. Res. Reports*, vol. 4, no. 1, pp. 1–24, 2019, doi: 10.9734/JERR/2019/v4i116891.

[51] H. Ræder *et al.*, "Taking piezoelectric microsystems from the laboratory to production," *J. Electroceramics*, vol. 19, no. 4, pp. 357–362, Dec. 2007, doi: 10.1007/s10832-007-9036-3.

[52] R. H. T. Wilke, P. J. Moses, P. Jousse, C. Yeager, and S. Trolier-McKinstry, "Wafer mapping of the transverse piezoelectric coefficient, e 31,f, using the wafer flexure technique with sputter deposited Pt strain gauges," *Sensors Actuators, A Phys.*, vol. 173, no. 1, pp. 152–157, 2012, doi: 10.1016/j.sna.2011.10.030.

[53] M. K. Tripp, C. Stampfer, C. F. Herrmann, C. Hierold, S. George, and V. M. Bright, "Low stress atomic layer deposited alumina for nano electro mechanical systems," in *Digest of Technical Papers - International Conference on Solid State Sensors and Actuators and Microsystems, TRANSDUCERS '05*, 2005, vol. 1, pp. 851–854, doi: 10.1109/SENSOR.2005.1496551.

[54] R. Ross, "Graphical methods for plotting and evaluating Weibull distributed data," in *Proceedings of 1994 4th International Conference on Properties and Applications of Dielectric Materials (ICPADM)*, 2002, vol. 1, pp. 250–253, doi: 10.1109/icpadm.1994.413986.

[55] J. B. Quinn and G. D. Quinn, "A practical and systematic review of Weibull statistics for reporting strengths of dental materials," *Dent. Mater.*, vol. 26, no. 2, pp. 135–147, 2010, doi: 10.1016/j.dental.2009.09.006.

[56] R. V. Wang and P. C. McIntyre, "O 18 tracer diffusion in Pb (Zr,Ti) O3 thin films: A probe of local oxygen vacancy concentration," *J. Appl. Phys.*, vol. 97, no. 2, Jan. 2005, doi: 10.1063/1.1814813.

[57] J. Robertson, W. L. Warren, B. A. Tuttle, D. Dimos, and D. M. Smyth, "Shallow Pb3+ hole traps in lead zirconate titanate ferroelectrics," *Appl. Phys. Lett.*, vol. 63, no. 11, pp. 1519–1521, 1993, doi: 10.1063/1.110761.

[58] M. V. Raymond and D. M. Smyth, "Defects and charge transport in perovskite ferroelectrics," *J. Phys. Chem. Solids*, vol. 57, no. 10, pp. 1507–1511, 1996, doi: 10.1016/0022-3697(96)00020-0.

[59] H. C. Ling and A. M. Jackson, "Correlation of Silver Migration with Temperature-Humidity-Bias (THB) Failures in Multilayer Ceramic Capacitors," *IEEE Trans. Components, Hybrids, Manuf. Technol.*, vol. 12, no. 1, pp. 130–137, Mar. 1989, doi: 10.1109/33.19027.

[60] A. Warren, A. Nylund, and I. Olefjord, "Oxidation of tungsten and tungsten carbide in dry and humid atmospheres," *Int. J. Refract. Met. Hard Mater.*, vol. 14, no. 5–6, pp. 345–353, 1996, doi: 10.1016/S0263-4368(96)00027-3.

[61] T. Shinagawa, A. T. Garcia-Esparza, and K. Takanabe, "Insight on Tafel slopes from a microkinetic analysis of aqueous electrocatalysis for energy conversion," *Sci. Rep.*, vol. 5, no. May, pp. 1–21, 2015, doi: 10.1038/srep13801.

[62] C. Zhang, H. He, and K. ichi Tanaka, "Catalytic performance and mechanism of a Pt/TiO2catalyst for the oxidation of formaldehyde at room temperature," *Appl. Catal. B Environ.*, vol. 65, no. 1–2, pp. 37–43, 2006, doi: 10.1016/j.apcatb.2005.12.010.

[63] L. J. LeGore, R. J. Lad, J. F. Vetelino, B. G. Frederick, and E. A. Kenik, "Aggregation and sticking probability of gold on tungsten trioxide films," in *Sensors and Actuators, B: Chemical*, 2001, vol. 76, no. 1–3, pp. 373–379, doi: 10.1016/S0925-4005(01)00638-4.

[64] M. Daté and M. Haruta, "Moisture effect on CO oxidation over Au/TiO2 catalyst," *J. Catal.*, vol. 201, no. 2, pp. 221–224, Jul. 2001, doi: 10.1006/jcat.2001.3254.

[65] S. J. Ippolito, S. Kandasamy, K. Kalantar-Zadeh, and W. Wlodarski, "Hydrogen sensing characteristics of WO3 thin film conductometric sensors activated by Pt and Au catalysts," in *Sensors and Actuators,*

B: Chemical, 2005, vol. 108, no. 1-2 SPEC. ISS., pp. 154–158, doi: 10.1016/j.snb.2004.11.092.

[66] M. Gotić, M. Ivanda, S. Popović, and S. Musić, "Synthesis of tungsten trioxide hydrates and their structural properties," *Mater. Sci. Eng. B Solid-State Mater. Adv. Technol.*, vol. 77, no. 2, pp. 193–201, Aug. 2000, doi: 10.1016/S0921-5107(00)00488-8.

[67] D. Zheng, J. Swingler, and P. Weaver, "Current leakage and transients in ferroelectric ceramics under high humidity conditions," *Sensors Actuators A Phys.*, vol. 158, pp. 106–111, 2010.

[68] I. A. Ryzhkin, M. I. Ryzhkin, A. M. Kashin, E. A. Galitskaya, and V. V. Sinitsyn, "High proton conductivity state of water in nanoporous materials," *EPL (Europhysics Lett.*, vol. 126, no. 3, p. 36003, Jun. 2019, doi: 10.1209/0295-5075/126/36003.

[69] N. Domingo *et al.*, "Surface charged species and electrochemistry of ferroelectric thin films," *Nanoscale*, vol. 11, no. 38, pp. 17920–17930, Oct. 2019, doi: 10.1039/c9nr05526f.

[70] S. Ø. Stub, E. Vøllestad, and T. Norby, "Mechanisms of Protonic Surface Transport in Porous Oxides: Example of YSZ," *J. Phys. Chem. C*, vol. 121, no. 23, pp. 12817–12825, 2017, doi: 10.1021/acs.jpcc.7b03005.

[71] W. P. Chen *et al.*, "Spontaneous recovery of hydrogen-degraded TiO_2 ceramic capacitors," *Appl. Phys. Lett.*, vol. 84, no. 1, pp. 103–105, Jan. 2004, doi: 10.1063/1.1637942.

[72] M. Promsawat, M. Deluca, S. Kampoosiri, B. Marungsri, and S. Pojprapai, "Electrical fatigue behavior of lead zirconate titanate ceramic under elevated temperatures," *J. Eur. Ceram. Soc.*, vol. 37, no. 5, pp. 2047–2055, May 2017, doi: 10.1016/j.jeurceramsoc.2016.12.037.

[73] D. Damjanovic, "Ferroelectric, dielectric and piezoelectric properties of ferroelectric thin films and ceramics," *Rep. Prog. Phys*, vol. 61, no. 9, pp. 1267–1324, 1998.

[74] A. Mazzalai, D. Balma, N. Chidambaram, R. Matloub, and P. Muralt, "Characterization and Fatigue of the Converse Piezoelectric Effect in PZT Films for MEMS Applications," *J. Microelectromechanical Syst.*, vol. 24, no. 4, pp. 831–838, 2015, doi: 10.1109/JMEMS.2014.2353855.

[75] Y. A. Genenko, J. Glaum, M. J. Hoffmann, and K. Albe, "Mechanisms of aging and fatigue in ferroelectrics," *Materials Science and Engineering B: Solid-State Materials for Advanced Technology*, vol. 192, no. C. Elsevier, pp. 52–82, 01-Feb-2015, doi: 10.1016/j.mseb.2014.10.003.

[76] D. Jiang, C. Pierre, and S. W. Shaw, "Nonlinear normal modes for vibratory systems under harmonic excitation," *J. Sound Vib.*, vol. 288, no. 4–5, pp. 791–812, 2005, doi: 10.1016/j.jsv.2005.01.009.

[77] S. Tiwari and R. N. Candler, "Using flexural MEMS to study and exploit nonlinearities: a review," *J. Micromechanics Microengineering*, vol. 29, no. 8, p. 083002, Aug. 2019, doi: 10.1088/1361-6439/ab23e2.

[78] D. Antonio, D. H. Zanette, and D. López, "Frequency stabilization in nonlinear micromechanical oscillators," *Nat. Commun.*, vol. 3, no. May, 2012, doi: 10.1038/ncomms1813.

[79] Y. Yang *et al.*, "Nonlinearity of Degenerately Doped Bulk-Mode Silicon MEMS Resonators," *J. Microelectromechanical Syst.*, vol. 25, no. 5, pp. 859–869, Oct. 2016, doi: 10.1109/JMEMS.2016.2586099.

[80] V. Kaajakari, T. Mattila, A. Lipsanen, and A. Oja, "Nonlinear mechanical effects in silicon longitudinal mode beam resonators," *Sensors Actuators, A Phys.*, vol. 120, no. 1, pp. 64–70, 2005, doi: 10.1016/j.sna.2004.11.010.

[81] A. K. E. Andersson, S. M. Selbach, C. S. Knee, and T. Grande, "Chemical expansion due to hydration of proton-conducting perovskite oxide ceramics," *J. Am. Ceram. Soc.*, vol. 97, no. 8, pp. 2654–2661, Aug. 2014, doi: 10.1111/jace.12990.

[82] L. M. Denis, G. Esteves, J. Walker, J. L. Jones, and S. Trolier-McKinstry, "Thickness dependent response of domain wall motion in declamped {001} Pb(Zr_0.3Ti_0.7)O_3 thin films," *Acta Mater.*, vol. 151, pp. 243–252, Jun. 2018, doi: 10.1016/j.actamat.2018.03.046.

[83] M. D. Nguyen, E. P. Houwman, M. Dekkers, and G. Rijnders, "Strongly Enhanced Piezoelectric Response in Lead Zirconate Titanate Films with Vertically Aligned Columnar Grains," *ACS Appl. Mater. Interfaces*, vol. 9, no. 11, pp. 9849–9861, 2017, doi: 10.1021/acsami.6b16470.

[84] L. Lian and N. R. Sottos, "Stress effects in sol-gel derived ferroelectric thin films," *J. Appl. Phys.*, vol. 95, no. 2, pp. 629–634, 2004, doi: 10.1063/1.1632019.

[85] C. Yan, Y. Minglei, Z. Qunying, C. Xiaolong, C. Jinkui, and G. Le, "Properties of RF-sputtered PZT thin films with Ti/Pt electrodes," *Int. J. Polym. Sci.*, vol. 2014, 2014, doi: 10.1155/2014/574684.

[86] S. Jeon and T. Thundat, "Instant curvature measurement for microcantilever sensors," *Appl. Phys. Lett.*, vol. 85, no. 6, pp. 1083–1084, Aug. 2004, doi: 10.1063/1.1781389.

[87] A. Mazzalai, D. Balma, N. Chidambaram, P. Muralt, L. Colombo, and T. Schmitz-Kempen, "Dynamic and long-time tests of the transverse piezoelectric coefficient in PZT thin films," in *ISAF/IWATMD/PFM 2014*, 2014, pp. 1–4, doi: 10.1109/ISAF.2014.6922998.

[88] M. Deluca, R. Bermejo, M. Pletz, M. Wießner, P. Supancic, and R. Danzer, "Influence of deposited metal structures on the failure mechanisms of silicon-based components," *J. Eur. Ceram. Soc.*, vol. 32, no. 16, pp. 4371–4380, Dec. 2012, doi: 10.1016/j.jeurceramsoc.2012.06.027.

[89] K. Coleman, R. Bermejo, D. Leguillon, and S. Trolier-McKinstry, "Thickness Dependence of Crack Initiation and Propagation in Piezoelectric Microelectromechanical Stacks," *Acta Mater.*

[90] M. Suermann, T. Kiupel, T. J. Schmidt, and F. N. Büchi, "Electrochemical Hydrogen Compression: Efficient Pressurization Concept Derived from an Energetic Evaluation," *J. Electrochem. Soc.*, vol. 164, no. 12, pp. F1187–F1195, 2017, doi: 10.1149/2.1361712jes.

[91] M. Wu *et al.*, "Tuning the ferroelectric and piezoelectric properties of 0.91Pb(Zn 1/3Nb2/3)O3-0.09PbTiO3 single crystals and lead zirconate titanate ceramics by doping hydrogen," *J. Phys. Chem. C*, vol. 114, no. 21, pp. 9955–9960, Jun. 2010, doi: 10.1021/jp101463e.

[92] H. Y. Huang, W. Y. Chu, Y. J. Su, K. W. Gao, J. X. Li, and L. J. Qiao, "Hydrogen-induced semiconductor transformation of lead zirconate titanate ferroelectric ceramics," *J. Am. Ceram. Soc.*, vol. 90, no. 7, pp. 2062–2066, Jul. 2007, doi: 10.1111/j.1551-2916.2005.00871.x.

[93] L. W. Li, X. Sun, J. X. Li, L. J. Qiao, Y. J. Su, and W. Y. Chu, "Effect of humidity on subcritical crack growth of indentation crack under sustained electric field in PZT ceramics," *Appl. Surf. Sci.*, vol. 255, no. 18, pp. 7841–7845, 2009, doi: 10.1016/j.apsusc.2009.02.052.

[94] E. Vereshchagina, E. Poppe, K. Schjolberg-Henriksen, M. Wohrmann, and S. Moe, "Metal Films for MEMS Pressure Sensors: Comparison of Al, Ti, Al-Ti Alloy and Al/Ti Film Stacks," in *2018 7th Electronic System-Integration Technology Conference, ESTC 2018 - Proceedings*, 2018, pp. 1–9, doi: 10.1109/ESTC.2018.8546422.

[95] N. Bassiri-Gharb, I. Fujii, E. Hong, S. Trolier-Mckinstry, D. V Taylor, and D. Damjanovic, "Domain wall contributions to the properties of piezoelectric thin films," *J. Electroceramics*, vol. 19, no. 1, pp. 47–65, 2007, doi: 10.1007/s10832-007-9001-1.

[96] Y. A. Genenko and D. C. Lupascu, "Drift of charged defects in local fields as aging mechanism in ferroelectrics," *Phys. Rev. B - Condens. Matter Mater. Phys.*, vol. 75, no. 18, 2007, doi: 10.1103/PhysRevB.75.184107.

[97] F. Chen, R. Schafranek, W. Wu, and A. Klein, "Formation and modification of Schottky barriers at the PZT/Pt interface," *J. Phys. D. Appl. Phys.*, vol. 42, no. 21, p. 215302, Nov. 2009, doi: 10.1088/0022-3727/42/21/215302.

[98] A. Klein, "Interface Properties of Dielectric Oxides," *J. Am. Ceram. Soc.*, vol. 99, no. 2, pp. 369–387, 2016, doi: 10.1111/jace.14074.

[99] T. J. M. Bayer *et al.*, "The relation of electrical conductivity profiles and modulus data using the example of STO:Fe single crystals: A path to improve the model of resistance degradation," *Acta Mater.*, vol. 117, pp. 252–261, 2016, doi: 10.1016/j.actamat.2016.07.024.

[100] G. W. Dietz, W. Antpöhler, M. Klee, and R. Waser, "Electrode influence on the charge transport through SrTiO3 thin films," *J. Appl. Phys.*, vol. 78, no. 10, pp. 6113–6121, 1995, doi: 10.1063/1.360553.